Pharmacokinetic Analysis of Gd-DTPA Enhancement in Dynamic Three-Dimensional MRI of Breast Lesions

Jacques A. den Boer, PhD • Ruud K.K.M. Hoenderop, MD • Jouke Smink, Msc • Gerard Dornseiffen, MD
Paul W.A.A. Koch, MD • Jan H. Mulder, MD, PhD • Cornelis H. Slump, PhD • Edo D.P. Volker, MD
Rob A.I. de Vos, MD

The purpose of this study was to demonstrate that dynamic MRI covering both breasts can provide sensitivity for tumor detection as well as specificity and sensitivity for differentiation of tumor malignancy. Three-dimensional gradient echo scans were used covering both breasts. Before Gd-DTPA bolus injection, two scans were obtained with different flip angles, and after injection, a dynamic series followed. Thirty-two patients were scanned according to this protocol. From these scans, in addition to enhancement, the value of T1 before injection was obtained. This was used to estimate the concentration of Gd-DTPA as well as the pharmacokinetic parameters governing its time course. Signal enhancement in three-dimensional dynamic scanning was shown to be a sensitive basis for detection of tumors. In our series, all but two mammographically suspicious lesions did enhance, and in three cases, additional enhancing lesions were found, two of which were in the contralateral breast. The parameter most suited for classification of breast lesions into benign or malignant was shown to be the pharmacokinetically defined permeability k_{31}, which, for that test, gave a sensitivity of 92% and a specificity of 70%. Our three-dimensional dynamic MRI data are sensitive for detection of mammographically occult breast tumors and specific for classification of these as benign or malignant.

Index terms: Magnetic resonance imaging • Gd-DTPA • Pharmacokinetics
Breast lesions

JMRI 1997; 7:702–715

From the Medisch Spectrum Twente, Department of MRI Research, Haaksbergerstraat 55, 7513 ER Enschede, The Netherlands (J.A.B., R.K.K.M.H., G.D., P.W.A.A.K., J.H.M., E.D.P.V); the University of Twente, Department of Electrical Engineering, Enschede, the Netherlands (J.S., C.H.S.); and the Regional Pathology laboratory, Enschede, the Netherlands (R.A.I.V.). Received July 15, 1996; revision requested December 16; revision received February 21, 1997; accepted March 10. Supported by a grant of Philips Medical Systems. Part of this work was presented at the meeting of the Society for Magnetic Resonance Imaging, Dallas, 1994. **Address correspondence to** J.A.B., Zweerslaan 3, 6591 GN Son, The Netherlands. E-mail: denboer@iaehv.nl.

Abbreviations: DCIS = ductal carcinoma in situ, FFE = fast field echo, fom = figure of merit, Gd-DTPA = gadolinium diethylenetriamine pentaacetic acid, NSA = number of signals averaged, ROC = receiver operating characteristic, ROI = region of interest.

DIAGNOSIS OF BREAST LESION malignancy usually is based on core biopsy guided by x-ray mammography or ultrasound. However, there are classes of patients for whom such a method is not optimal. This, for example, is the case when a lesion is small, multifocal, or not well delineated. In such cases, surgical biopsy would be needed. For reduction of patient morbidity and financial expense, it would be desirable to avoid unnecessary biopsies by a noninvasive test that is sensitive for lesion detection as well as specific for distinction between benign and malignant. Additionally, such a test could be of value for follow-up studies of breast lesions after lumpectomy or chemotherapy.

Contrast-enhanced MRI may be suitable for these purposes (1–24). Rapid enhancement of the signal in postcontrast images is strongly indicative of the presence of a lesion. This can be observed when the scan is repeated as a dynamic series (1–10,14–16,19–24). However, the reported specificity for classification of breast lesions as benign or malignant is not always satisfactory (5,7,10–12).

In some of the quoted literature (11–16,21), the scan methods are aimed at the detection of contrast enhancement in the complete breast. The scans used by Heywang et al (11), Harms et al (12), and Perman et al (15) cover one entire breast; those of Rigauts (13) cover both breasts. In these cases, the MRI examination can be used for detection of occult lesions. Sensitivity of the MRI examination in this respect is shown to be important because of the potential presence of lesion multifocality (12) or when lesion location is uncertain (13,15). At high spatial resolution of $1 \times 1 \times 5$ mm^3 (11) or $1 \times 1 \times 1$ mm^3 (12), lesion detection sensitivity is found to be close to 100% for cases that already are suspected on the basis of x-ray mammography. However, in these last reports, the temporal resolution was low (300 seconds per scan) and differentiation between benign and malignant was not adequately possible.

In studies by Perman et al (15) and Hulka et al (21), an approach is presented in which enhancement is inspected dynamically with a much higher temporal resolution, 44 seconds (15) and 6 seconds (21), while the entire breast is covered at the same time. Such an approach is attractive when detection sensitivity as well as specificity for tumor classification are both required. To reach sufficient temporal resolution, in these reports, a three-dimensional scan technique was used with a moderate spatial resolution (pixel size is $3 \times 1 \times 2$ mm^3 in one breast (15) and $7 \times 1.5 \times 3$ mm^3 in both breasts (21)). In the present study, this approach is used as well and our scan is a dynamic scan that covers both breasts with a temporal resolution of 30 seconds and spatial resolution of $6 \times 1.3 \times 1.7$ mm^3.

A more advanced data analysis is possible (16–24) when the enhancement-time courses are converted to concentration-time courses, using the precontrast relaxation time T1 (in this report called the native T1). In such an approach, the enhancement is replaced by the contrast medium concentration, thereby removing the influence of this tissue property from the data. In the present study, accordingly, the native T1 is determined for each patient and each enhancement factor is reduced to gadolinium diethylenetriamine pentaacetic acid (Gd-DTPA) concentration.

In addition, in the same reports, the shape of the concentration-time course is modeled as a pharmacokinetic curve. In these models, the leakage of the contrast agent into the interstitial space is seen as the cause of the signal enhancement. Hulka et al (21) demonstrated statistically that the derived pharmacokinetic parameter, when compared with signal enhancement, improves the degree of separation between malignant and benign breast lesions, but they do not show whether this improvement is due to their correction for T1 or to their pharmacokinetic modeling. To inspect the potential of this approach, we have fitted the dynamic T1 corrected MR data to a pharmacokinetic model, derived from that of Tofts et al (20,22) and obtained model parameters.

The purpose of our work is to determine the sensitivity for tumor detection obtained with our three-dimensional dynamic contrast-enhanced MRI scan, given its moderate spatial resolution. Next, we want to find the sensitivity and specificity for classification of lesions as benign or malignant that can be reached with our data and the contribution of each of the two steps that we have taken in data reduction: correction of the enhancement data for native T1 and pharmacokinetic curve fitting.

• MATERIALS AND METHODS

Patients

Thirty-two patients participated in the study on a voluntary basis. These patients were chosen when mammographic images gave reason to suspect a malignancy, and for each patient, the decision already had been made that biopsy was needed. The first group of 15 patients (age range, 50–70 years; mean age, 57 years) consisted of clients from the Dutch mass population screening. In this group, only women who had nonpalpable lesions were included. The second group of 17 patients (age range, 30–80 years; mean age, 53 years) consisted of symptomatic patients who presented without previous breast tumor treatment and for whom surgical biopsy was planned. The study protocol was accepted by the Ethical Committee of our institution. The MRI examination always was carried out before biopsy. However, this result was not permitted to influence the course of the patients' treatment.

X-Ray Mammography and Histology

All x-ray examinations were performed with a Senograph 600 I mammography system (CGR, Paris, France), using craniocaudal, oblique, and mediolateral views. A biopsy was obtained from all mammographically suspicious lesions. Biopsy locations were guided by the x-ray mammographic results. In all cases, the specimen was removed surgically. After its entire surface had been inked to facilitate microscopic recognition of the surgical edges, it was sectioned at 5-mm intervals and of each part an x-ray image was taken. These images were used during the surgical procedure to confirm that the suspected tissue was contained in the specimen. Tissue blocks for paraffin microscopy sections were then obtained of all grossly and mammographically suspicious areas.

MRI

MR images were obtained with a Gyroscan ACS MRI system (Philips Medical Systems, Eindhoven, the Netherlands) operating at 1.5 T. The patients were positioned prone with both breasts placed in a recess in a linear receive-only surface coil. The coil design restricted motion of the breast tissue in the craniocaudal direction. After a preliminary scan for localization, all scans were made in the axial direction with a field of view of 320 mm. For all scans, a spoiled gradient echo method, T1-enhanced fast field echo (T1-FFE), and three-dimensional encoding were used. For each scan, 36 partitions of 6 mm thick and 3-mm overlap (Fourier interpolation) were obtained. In this way, the scanned volume had a thickness of 108 mm and covered all space in the coil recess. The phase-encode gradient was left to right, so that the movement artefact of the heart did not cross the breasts, except for the extreme axillary regions. The scan parameters of the first of the T1-FFE scans were as follows: TR/TE = 16/9 msec, flip angle = 4°, acquisition matrix $nz \times ny \times nx = 18 \times 192 \times 256$; number of signals averaged (NSA) = 2. The value of TE was the lowest in-phase value obtainable in our system. This scan was made to allow calculation of the native relaxation time T1 (see Appendix B). The subsequent seven scans were a dynamic series with the same scan parameters, except for the flip angle (40°) and NSA (1). In the dynamic series, the duration of each scan was 30 seconds, which was the minimum that could be achieved with the number of slices and the matrix size. A half scan technique and an elliptic coverage of the k plane[1] were used for scan time reduction. The half scan technique was used in the k_y direction. Within each scan, the k_y and k_z values were changed in linear order in a nested loop with the k_y values varying in the inner loop. This caused the moment at which both k_y and k_z were zero to occur at a time halfway through each scan. That moment, 15 seconds after the start of each scan, is the one that best characterizes the dynamic situation that is described in the image. We will call this moment the characteristic time *tc* of the scan.

Before the start of the scans, an injection needle was inserted in the cubital vein in the right antecubital fossa.

1 Elliptic coverage of the k space is possible in three-dimensional acquisition without visible loss of spatial resolution by removing the combination of large k_y and k_z values. The result is a gain in scan time of approximately 22%.

A syringe with 7.5 mmol of Gd-DTPA (Magnevist; Schering, Berlin, Germany; 15 ml) was connected with the needle via a 15-ml cannula filled with physiologic saline. This setup allowed injection during the dynamic series without movement of the patient.

The start times of the dynamic scans were *ts* = 0, 50, 80, 140, 210, 280, and 350 seconds. Completion of the first scan was the sign for the radiologist to start injection. The syringe was emptied into the cannula in approximately 5 seconds, and the tube was then flushed with 25 ml of saline in another 5 seconds. Therefore, a bolus of contrast medium entered the body starting at 5 seconds after the end of the first dynamic scan. The transport time *tt* of the contrast medium from the site of injection to the breast was estimated to be 15 seconds. This equals the mean delay to peak of the digital subtraction angiography signal as observed in the carotids in intravenously-injected iodine contrast studies (25) (for discussion of the error in this estimate, see Appendix D). As a result, the nominal arrival time of the bolus coincided with the start time of the second dynamic scan (*ts* = 50 seconds). This time was taken as the zero point of the pharmacokinetic time scale. On this scale, the characteristic times of the remainder scans were at:

$$t = (ts - 50) + tc = (ts - 35) \text{ seconds}$$

Lesion Detection

For lesion detection, the two three-dimensional sets of preinjection images (small and large flip angle) were presented to the radiologist, along with subtraction images that were made from the first and the second postinjection scan, using the preinjection scan of the dynamic series as a mask. Detection of lesions was based on visual inspection of these MR images and correlation of the findings to x-ray mammography. All mammographic suspicious lesions could be found confidently by visual inspection of the images. All slices with visually apparent lesions were subjected to numeric analysis.

The numeric analysis of the MRI data was performed on a workstation on each of the slices selected by the radiologist. To correct for motion of the patient between the scans, when necessary, the images (eight images of each slice) were registered with the help of a two-dimensional shift tool. Shifts were possible in steps as small as .1 times the pixel size. The tool required operator supervision to select the most satisfactory shift. Although subjective, the process was reproducible within .3 pixels, as tested by comparing the shift obtained by two different observers.

Objective and automatic definition of enhancing regions was based on comparison of the actual enhancement-time course of each pixel to a typical reference course. To do so, the images of the dynamic scan were reduced to a single weighted sum image. The technique used for this reduction is derived from eigen image filtering (26) and discussed in Appendix A. The reference enhancement values are listed in Table A1. In the weighted sum image, the pixel values are high when there is a close match between the actual and the reference enhancement-time course. To define the enhancing region, the weighted sum image was thresholded at 75% of its maximum pixel value. When no supra threshold region resulted, the threshold was reduced to 50 % and, if necessary, to 30%. Regions smaller than 8 connected pixels were rejected to avoid misreadings from data that were strongly distorted by partial volume effects.

The sensitivity of detection of the lesions by enhancement was obtained by comparing the generated enhancing regions with the visually ascertained lesions. Moreover, the enhancing regions were used to define mean values for each of the parameters derived per pixel.

In a few cases with very low enhancement, no enhancing region showed up in the automated procedure. Then, the lesion was considered to be nonenhancing and, for evaluation of mean parameter values, a region of interest (ROI) corresponding to the visual area of the lesion was defined manually.

Parameters Obtained per Pixel

From the ratio of the two precontrast scans, the relaxation time of the native tissue ($T1_N$) was calculated with help of Equations [B1] and [B2] in Appendix B. The scans had a constant scale so that all signal values for each pixel were directly physically comparable. For each pixel, the ratios of the postcontrast and precontrast scans of the dynamic series defined six enhancement factors. With Equations [B1] and [B3], the Gd-DTPA concentrations per pixel could be derived from these enhancement factors and $T1_N$. The enhancement factor observed for the third dynamic scan (at t = 45 seconds) and the corresponding concentration were recorded for later use and were called *Enh(45)* and *Gd(45)*.

A pharmacokinetic model similar to that of Tofts et al (22) was used to describe the time course of the contrast medium concentration. The model and its assumptions are discussed in Appendix C. Three parameters are obtained: f_1, the fractional volume of the vascular space; f_3, that of the leakage space; and k_{31}, the permeability of the boundary between plasma and leakage space.

The modeled signal enhancement was fitted to the data by adjustment of these parameters. This was based on minimization of the squared differences between the modeled and the observed enhancement factors (Levenberg Marquardt method). The mean value of the residual squared differences, normalized to image noise (see Table D1), was used as a figure of merit (fom) for the fit.

Statistical Analysis

Per enhancing region, a mean value was obtained for each of the parameters, $T1_N$, *Enh(45)*, *Gd(45)*, f_1, f_3, and k_{31}, by averaging over all pixels in that region. When more than one enhancing region was present in one lesion (the lesion was, for example, seen in more than one slice), all enhancing regions were analyzed. The parameter values belonging to the region with the highest mean k_{31} were used to describe the lesion. Statistical significances of these MRI-based lesion parameters were obtained by comparing histology. For some of the parameters, receiver operating characteristic (ROC) curves and scatter diagrams were used to inspect their suitability for lesion classification.

• RESULTS

Figure 1 shows some of the images obtained for a patient with a large phyllodes tumor (case 4). Details describing how these images were reached are given in the legend of this figure. The signal-to-noise ratio in the original MR images (Figs. 1a, 1b, and 1c) is approximately 2% of the unenhanced glandular signal. The area of enhancement at 45 seconds (Fig. 1c) is rather homogeneous and its visual contour has a fair correspondence to that selected by our automatic procedure (Figs. 1f, 1g, and 1h).

Figure 2 shows examples of observed enhancement factors as function of time. The enhancement factors shown are the mean values per enhancing region. Per case, the

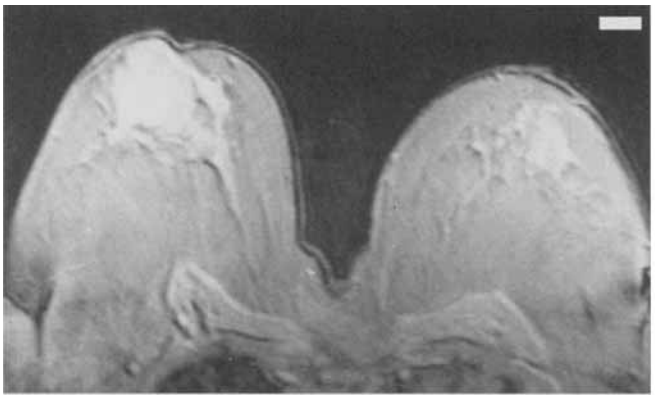

a.

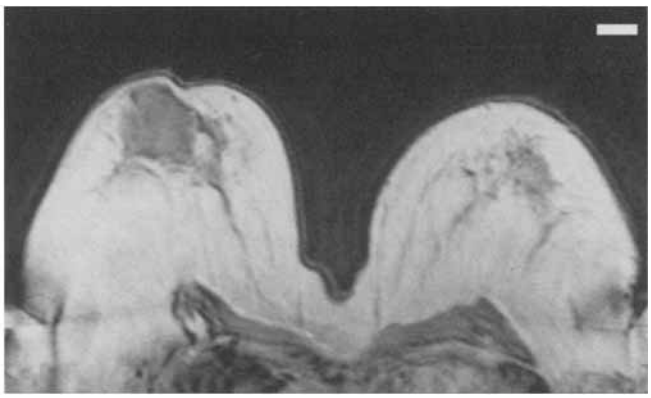

b.

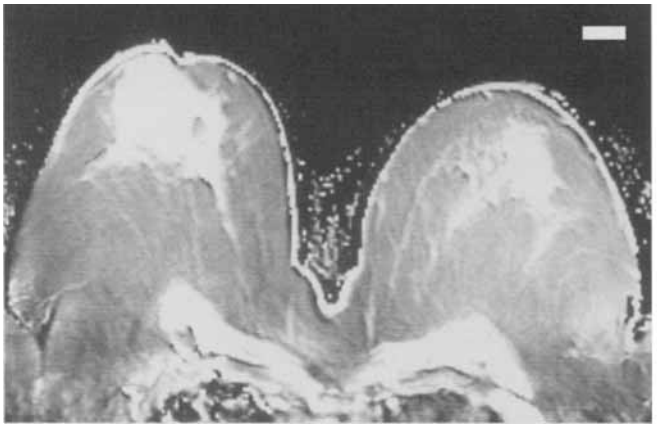

c.

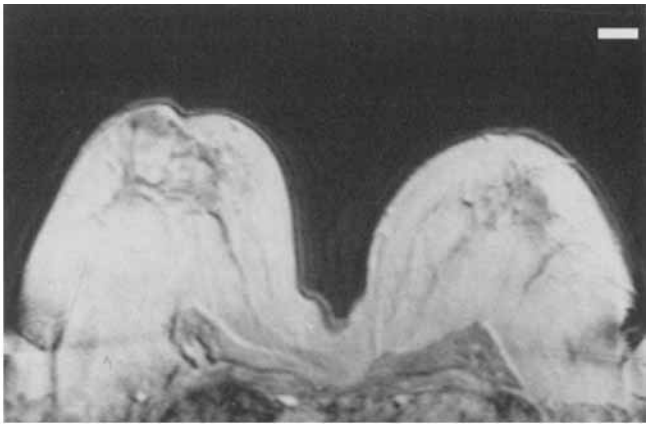

d.

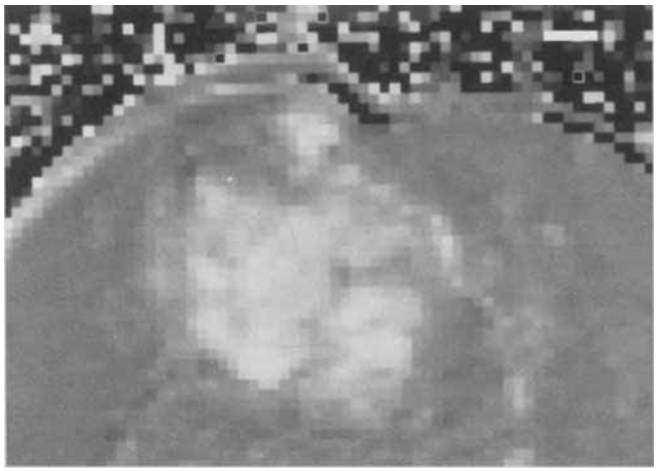

e.

Figure 1. Case 4: a 61-year-old patient with a large phyllodes tumor. All images are of the same slice: slice 16 of 36. In the parameter maps, the gray values are approximately proportional to the values of the parameter mapped. Calipers indicate the relative magnification of each image. An enhancement-time curve for this case is given in Figure 2. (**a**) Pre bolus scan; T1-FFE; TR = 16, TE = 9, flip angle = 4. (**b**) First scan of the dynamic series, before bolus arrival; T1-FFE; TR = 16, TE = 9, flip angle = 40. (**c**) Parameter map of native T1, from images (**a**) and (**b**). (**d**) Scan at 45 seconds after bolus arrival. The left breast shows an enhancing lesion. (**e**) Image of enhancement factors at 45 seconds; ratio of image (**d**) and (**b**); area of the left breast, enlarged.

best fitting pharmacokinetic model-based enhancement-time curve is drawn for comparison. Two benign cases are shown in Figure 2a and two malignant cases are shown in Figure 2b. The model parameters and the fom for the fit of these curves are given in the figure caption. All curves in this figure fit within the error ranges, illustrating that our model did give an adequate description of the data. The mean fom for all fits (each pixel in the enhancing region, all patients) is 2.6.

Table 1 lists the demographic, mammographic, histologic, and MRI data for each patient. All MRI parameters are mean values over one enhancing region per lesion (the one for which highest mean k_{31} was found). The fraction of the tumor volume covered by this region was estimated to range from approximately 5% for large tumors to more than 50% for small tumors. All data for mammographically nonsuspicious lesions (no histology available) are printed in italics. The cases are arranged in order of histologic class and within each class in order of increasing k_{31}. In cases 5 and 8, the lesions did not visibly enhance in MRI. These lesions could be included for analysis after identification on basis of their conspicuity in the precontrast images. In case 18, the lesion was situated in the axillary region of the breast and part of it was in an area that was heavily corrupted because of flow artefacts emanating from the heart. In this case, the analysis was carried out on a manually defined ROI outside the artefact zone. One or more enhancing regions were found in 32 of 34 lesions, so that the sensitivity for tumor detection on basis of enhancement was 96%.

Data from Table 1 are summarized in Table 2 (lesions for which histology was available), which shows means

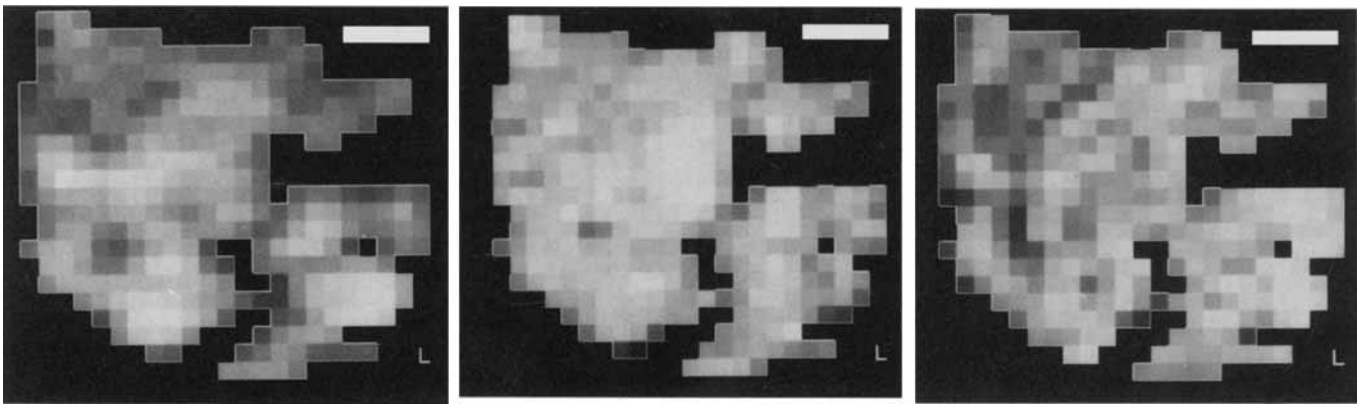

f. g. h.

Figure 1. *(Continued).* Images (**f**), (**g**), and (**h**) show only the enhancing region visible in (**d**) but bordered by automatic segmentation (see text). (**f**) Parameter map of vascular space f_1 (gray scale: $f_1 = 0...1$). (**g**) Parameter map of leakage space f_3 (gray scale: $f_3 = 0...1$). (**h**) Parameter map of permeability k_{31} (gray scale: $k_{31} = 0...100.10^{-3}$ sec^{-1}).

and SDs of $T1_N$, *Enh(45)*, *Gd(45)*, f_1, f_3, and k_{31} taken from Table 1 for the groups of benign and malignant cases. For comparison, corresponding values are shown for normal fat and normal glandular breast tissue. These were obtained from data of a group of seven normal breasts. Of particular interest are the differences of the parameter values between benign and malignant lesions. The statistical significance of these differences was tested with the Wilcoxon rank sum test and is given per parameter. Compared with benign lesions, malignant lesions had a significantly larger mean value of *Gd(45)*, f_1, and k_{31}. Of these, the difference in k_{31} has the highest significance ($P < .005$), followed by that in f_1 ($P < .02$).

In Figure 3, the observed values of *Enh(45)* and those of k_{31} for each patient are plotted as function of $T1_N$. *Enh(45)* was correlated significantly to $T1_N$ (correlation coefficient $c = .68$; $P > 99.9\%$). Linear regression showed that 46% of the variance in *Enh(45)* can be explained by its correlation to $T1_N$. The correlation between k_{31} and $T1_N$ was much smaller ($c = -.35$; $P < 95\%$).

Figure 4 shows ROC curves belonging to tests of tumor malignancy with some of the derived lesion parameters. In each curve, the true-positive rate is plotted against the false-positive rate with the threshold for testing as parameter and histology as gold standard. Shown are curves for *Enh(45)*, *Gd(45)*, and k_{31}. The ROC curve for k_{31} shows the largest true-positive rates, followed by the curve for *Gd(45)*.

Figure 5 shows scatter diagrams in which the lesion parameters used in Figure 4 are compared with histologic diagnosis. In these diagrams, for purpose of illustration, malignant in situ and malignant invasive lesions are presented as separate classes. Suggested threshold values are added to show the results of a tumor malignancy test based on each of the diagrams. Using for k_{31} a threshold of $14 \cdot 10^{-3}$ sec^{-1}, there are three false positives and two false negatives, so that for this combination of test parameter and threshold, the sensitivity for classification of malignant tumors is 92% and the specificity is 70%. Inspection of the individual false cases in Table 1 shows that one of the false-positive cases is a fibroadenoma and the other two are adenosis and adiponecrosis, both characterized by a low T1 and a low enhancement factor. The false-negative cases both were comedo-type ductal carcinomas in situ. Figure 5 suggests that the average k_{31} of ductal carcinoma in situ (DCIS) tumors may be different from that of invasive tumors, but the difference found was not significant.

Finally, Table 3 shows an overview of enhancing regions that did not correlate to mammographically detected lesions. In case 10, follow-up x-ray mammography 1 year after lumpectomy of the left breast did not show suspicious abnormalities in either breast. In case 11, both breasts were resected. In case 27, follow-up x-ray mammography 1 year later did not reveal an abnormality in the contralateral (right) breast.

• DISCUSSION

Quantitative Diagnosis

From the MR images, we extracted numeric data on signal enhancement and used these for diagnostic purpose. Such a quantitative diagnosis must be objectively based. To show how we achieved this, we have given a detailed account of the steps used in the data analysis. Arbitrary choices sometimes had to be made and these can influence the parameter values obtained. In this respect, the representation of the lesions by enhancing regions is important. The enhancing regions were selected by an objective criterion in the fastest enhancing part of the lesion. Because of lesion heterogeneity, the enhancing regions found in some patients were much smaller than the (visually apparent) lesion size. This is in line with a remark of Boetes et al (18), who discuss occasional large differences in size between the enhancing region and the lesion.

In the process of reduction of the data to a single diagnostic descriptor per lesion, the representativeness of this descriptor should not be lost. Is the enhancing region representative for the lesion as a whole? Gribbestad et al (19) argue that restriction to the maximally enhancing region is necessary for a specific diagnosis. We approximated this requirement by our definition of the enhancing regions and by our choice of reporting the parameter values of one enhancing region only. The representativeness of this choice is supported by the observation that the parameter values found for different enhancing regions belonging to the same lesion usually were similar.

Moreover, quantitative diagnostic information must be obtained with a sufficiently small measurement error. The enhancement factors per pixel have an accuracy about equal to the MR image noise (2%). The concentrations of Gd-DTPA are less accurate because of the error in calculation of $T1_N$ (15%) (see Appendix D). An assess-

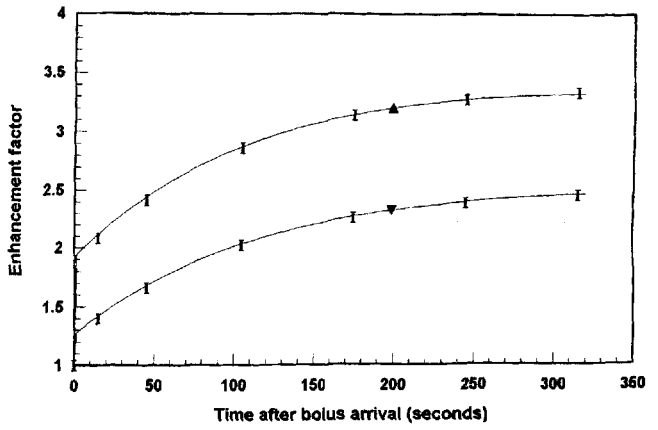

a.

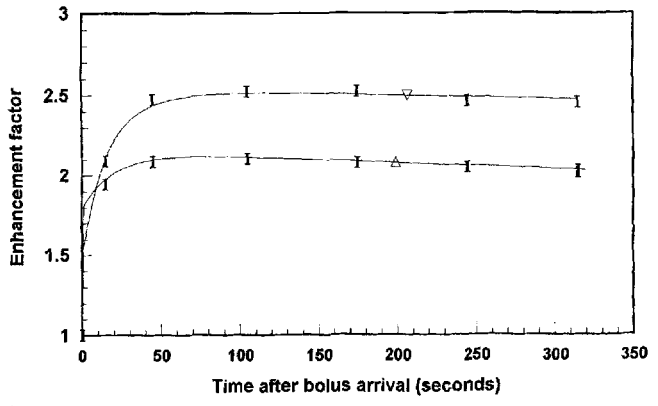

b.

Figure 2. Enhancement data of some cases and fits to these data of pharmacokinetic model-based enhancement-time curves. (**a**) Benign lesions. Case 4 (▲): images shown in Figure 1. Parameters for fit: $T1_N$ = 1.695 seconds; f_1 = .135, f_3 = .31, k_{31} = 7.3 · 10^{-3} sec^{-1}; fom = .13. Case 3 (▼): parameters for fit: $T1_N$ = 1.02 seconds, f_1 = .067, f_3 = .43, k_{31} = 6.4 × 10^{-3} sec^{-1}; fom = .41. (**b**) Malignant lesions. Case 28 (△): parameters for fit: $T1_N$ = .584 second, f_1 = .38, f_3 = .21, k_{31} = 46 · 10^{-3} sec^{-1}; fom = .11. Case 24: lesion R-1 (▽): parameters for fit: $T1_N$ = .645 second, f_1 = .12, f_3 = .64, k_{31} = 37 × 10^{-3} sec^{-1}; fom = 7.4 Error bars indicate the estimated signal inaccuracy per pixel (±2 SD). The fom of the fit in most of these figures is lower (better) than that of most fits per pixel, because of noise reduction by averaging the enhancement values over the ROI. Note that the parameters for fit given in the figure captions are not the same as those in Table 1. The difference arises because in this figure the fit is to the average of the enhancement factors per ROI, whereas in Table 1, the fit was obtained per pixel and the values given are the averages over the parameter values per pixel. As an example, enhancement values for case 3 are as follows:

Experimental	1.39	1.65	2.01	2.26	2.39	2.45
According to Table 1	1.43	1.70	2.05	2.27	2.38	2.43
According to Figure 2a	1.39	1.66	2.02	2.25	2.38	2.45

ment of the accuracy of the variables obtained with the pharmacokinetic model is discussed in Appendix D. The most important error sources were identified as the noise in the MR images, the uncertainty in the blood volume V_1, and the mean transit time of the contrast medium in the patient *tt*. The resulting errors in the pharmacokinetic parameters are summarized in Table D1. The table shows large errors for f_1 and f_3 but a relatively small error in k_{31}. Comparison of Table D1 and Table 2 shows that, for lesions, the observed distribution in f_1 and f_3 can be explained by measurement errors, but even per group of lesions, the distribution in T1 and k_{31} is significantly larger than the measurement error.

The relatively high accuracy of k_{31} (20%) was reached because there was only little propagation to this parameter of the errors in V_1 and *tt* (illustrated in Figure C2). V_1 relates to the ordinate scale and *tt* relates to its offset. Where f_1 and f_3 are influenced by the ordinate scale and its offset, k_{31} is a measure only of the curvature of the enhancement-time curves.

As a consequence, in our model, relatively accurate k_{31} values can be obtained without knowledge of the bolus arrival time per patient. Accuracy of k_{31} will be preserved as long as its value is smaller than $1/\Delta t$, the inverse of the time between the dynamic scans. For Δt = 30 seconds, this corresponds to $k_{31} < 33 \cdot 10^{-3}$ sec^{-1}. In our series, the mean k_{31} for benign lesions was $15 \cdot 10^{-3}$ sec^{-1} and for malignant lesions 35 × 10^{-3} sec^{-1} (see Table 2). The argument shows that the temporal resolution used in our dynamic scan was sufficient to resolve k_{31} in the range of interest.

Tumor Detection

A first important aspect of our results is that enhancement, as found in our data, is a reliable detection criterion for mammographically suspicious lesions with a detection sensitivity of 96%. This high sensitivity is relevant for detection of lesions not found before the MRI examination. Table 3 shows that in our series of three patients (10% of the cases) eight enhancing regions were found that were not suspicious in x-ray mammography. These new findings suggest the presence of additional lesions, although no histologic proof of their presence was obtained. (At the time of this study, MRI-guided biopsy support tools were not available.) Two of the patients with new findings entered through the population screening program. Moreover, two of the new findings were in the contralateral breast.

We used an axial slice orientation, which precluded inspection of the extreme axillary regions of the breasts because in these areas the images frequently were damaged by motion artefacts emanating from the beating heart. As an alternative, we could have used a sagittal scan (as was done in refs. 11, 12, and 15), more completely covering a single breast and at the same time allowing a smaller field of view and, therefore, a higher spatial resolution. Such changes in the scan technique potentially could have revealed smaller and more additional breast lesions but at the cost of loosing the coverage of both breasts.

The minimum lesion size detectable by our data analysis method equals the minimum size of the enhancing regions below which they are rejected. This size was 8 pixels, corresponding to a detection limit of about 6 × 6 × 6 mm^3. Scans with higher spatial resolution covering both breasts also would have been possible, but only at a lower temporal resolution of the dynamic scan. However, as discussed above, the temporal resolution used in our work is needed to allow assessment of the malignancy of the breast lesions. Harms and Flamig (12) concluded that 36% of malignant lesions detected with MRI were not found by x-ray mammography. This percentage of cases with new findings is higher than we found in our series. The reason may be related to the smaller voxel used in their study (1 × 1 × 1 mm^3), which is likely to correspond to a smaller detection limit, but in the cited study, the specificity for tumor classification was low.

Tumor Classification

The ROC curves of Figure 4 and the scatter diagrams of Figure 5 compare the degree of separation of malignant and benign lesions that can be obtained from the data. Testing of the lesions on *Enh(45)* is similar to the tests on

Table 1
Demographic, Mammographic, Histologic, and MRI Data per Case

Case No.	Age (years)	Client of Population Screening Program	Suspicious Lesions, Mammography	Early Enhancing Lesions, MRI	Histologic Diagnosis	Histologic Class	Enhancement at 45 seconds	Concentration at 45 seconds	$T1_N$ msec	f_1 (%)	f_3 (%)	$10^3 \cdot k_{31}$ (sec^{-1})
1	48	0	L1	L1	adenosis	0	2.16	0.28	1,250	16	64	3
2	68	0	L1	L1	trauma, fat necrosis	0	2.19	0.32	967	19	69	7
3	62	1	R1	R1	adenosis	0	1.69	0.16	1,083	6	43	7
4	61	1	R1	R1	phyllodes tumour	0	2.36	0.19	1,753	17	42	7
5	51	1	L1	—	fibroadenoma (sclerosing)	0	1.22	0.54	976	40	74	7
6	42	0	R1	R1	fibroadenoma, adenosis	0	2.29	0.5	767	24	66	11
7	44	0	L1	L1	fibroadenoma (intracanalicular)	0	3.24	0.21	2,629	14	29	12
8	56	0	R1	—	adiponecrosis	0	1.02	0.05	160	1	11	21
9	67	1	L1	L1	adenosis	0	1.4	0.22	475	7	43	27
10	43	0	L1	L1	fibroadenoma (pericanalicular)	0	3.08	0.37	1,023	24	35	49
			—	L2			*1.87*	*0.31*	*845*	*15*	*28*	*44*
			—	L3			*2.22*	*0.27*	*1,267*	*17*	*40*	*16*
			—	L4			*2.34*	*0.24*	*1,405*	*18*	*49*	*10*
			—	R1			*2.05*	*0.39*	*879*	*15*	*35*	*63*
11	57	0	L1	L1	DCIS comedo	1	2.34	0.36	1,029	23	48	9
			—	R1	ILC	1	*2.07*	*0.3*	*790*	*58*	*88*	*10*
			—	L2			*1.49*	*0.17*	*367*	*16*	*27*	*43*
12	63	1	R1	R1	DCIS comedo	1	1.42	0.34	525	11	51	12
13	53	0	R1	R1	DCIS comedo	1	2.58	0.31	1,454	24	24	15
14	49	1	L1	L1	DCIS comedo	1	1.99	0.34	778	30	37	16
15	50	1	R1	R1	DCIS comedo	1	1.85	0.39	620	16	34	17
16	35	0	L1	L1	IDC + DCIS comedo (EIC)	1	2.19	0.29	855	36	66	17
17	49	1	R1	L1	ILC + LCIS	1	1.76	0.29	729	20	35	20
18	50	0	L1	L1	DCIS comedo + (focal) IDC	1	2.87	0.71	1,025	46	45	20
19	55	1	L1	L1	ILC	1	2.67	0.4	1,398	32	26	20
20	32	0	L1	L1	IDC	1	3.61	0.37	1,948	21	34	24
21	67	0	L1	L1	IDC	1	2.57	0.39	1,211	34	39	27
22	51	0	L1	L1	IDC + DCIS noncomedo (EIC)	1	2.71	0.52	889	47	46	28
23	61	1	R1	R1	IDC	1	2.1	0.38	1,120	3	64	30
24	44	0	R1	R1	tubulolobular carcinoma	1	2.47	0.72	628	34	65	30
			R2	R2	tubulolobular carcinoma	1	2.1	0.71	515	22	61	67
			R3	R3	tubulolobular carcinoma	1	1.74	0.55	423	28	44	61
25	64	1	L1	L1	tubular carinoma + DCIS non comedo	1	2.12	0.33	908	21	13	31
26	57	1	L1	L1	DCIS comedo	1	2.59	0.38	1,125	35	28	37
27	51	1	L1	L1	LCIS + (multifocal) ILC	1	1.82	0.49	455	28	71	38
			—	R1			*2.11*	*0.62*	*1,060*	*12*	*30*	*40*
28	70	0	L1	L1	IDC	1	2.09	0.54	594	29	34	51
29	60	1	L1	L1	IDC + DCIS comedo (EIC)	1	3.01	0.46	1,117	14	41	54
30	80	0	L1	L1	IDC	1	2.88	0.74	728	20	72	65
31	68	1	R1	R1	IDC	1	2.06	0.22	1,176	22	13	66
32	59	0	R1	R1	DCIS comedo	1	1.54	0.62	284	9	63	80

Note.—DCIS, ductal carcinoma in situ; LCIS, lobular carcinoma in situ; IDC, invasive ductal carcinoma; EIC, IDC with extensive intraductal component; ILC, invasive lobular carcinoma. Histologic classes: 0 = benign, 1 = malignant. When more lesions were found in one patient, they are labeled for the left-sided and right-sided breast as L1, L2.., R1, R2, etc.

fast enhancement used frequently in the earlier literature (1–10). Inspection of the ROC curve for this parameter and of the corresponding scatter diagram in Figure 4a shows that for our data this approach is not very successful.

A first cause of the relative lack of specificity in testing to *Enh(45)* is illustrated in Figure B1, which shows from theory that this parameter depends on $T1_N$. This was pointed out already by Tofts et al (20) and Hulka et al (21). Experimental confirmation of this dependence as a strong correlation between these quantities is shown in Figure 3a.

Improved separation can be expected when the data are corrected for $T1_N$. This correction is obtained by conversion of enhancement into Gd-DTPA concentration. The improvement reached is illustrated by the ROC curve for *Gd(45)* in Figure 4 and in the scatter diagram of Figure 5b.

The use of k_{31} as a test criterion is suggested by Tofts et al (20) and by Hulka et al (21), who used for the same parameter the term "extraction flow product" (EF). Figure 3b shows that k_{31} has the required independence of $T1_N$. The ROC curve in Figure 4 for testing to k_{31} and the scatter diagram in Figure 5c show indeed a further improvement above that based on *Gd(45)*.

Table 2
Mean and SDs of Descriptors of Normal Breast Tissue and Lesions, Derived by Analysis of the MRI Data of Table 1

Tissue/Lesion Type	Cases	$T1_N$ (msec)	*Enh(45)*	*Gd(45)*	f_1 (%)	f_3 (%)	$k_{31} \cdot 10^3$ (sec^{-1})
Fat	7	410 ± 75	1.06 ± .1	.04 ± .02	4 ± 2	25 ± 10	13 ± 7
Gland	7	930 ± 300	1.25 ± .3	.07 ± .04	2 ± 1	20 ± 5	12 ± 6
Benign lesions	10	1110 ± 650	2.1 ± .7	.29 ± .15	17 ± 10	47 ± 19	15 ± 13
Malignant lesions	25	890 ± 370	2.3 ± .5	.45 ± .15	26 ± 12	45 ± 18	34 ± 20
Difference between benign and malignant*		ns	ns	$P < .02$	$P < .05$	ns	$P < .005$

Note.—Numbers given denote mean ± SD.
*Wilcoxon rank sum test; ns, not significant.

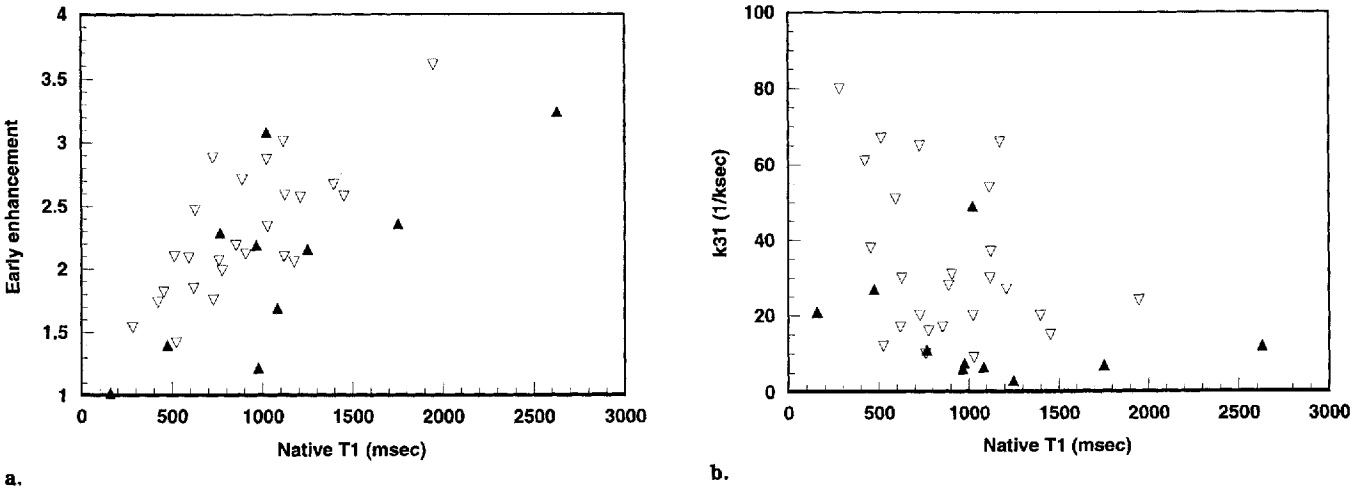

a. b.

Figure 3. (**a**) Graphical display of the distribution between patients of enhancement at 45 seconds plotted versus native T1 for benign (▲) and malignant (△) lesions. (**b**) Equivalent display, but of k_{31} versus native T1.

The areas under the ROC curves in Figure 4 were compared statistically in a paired test (27,29) and were shown to be not significantly different. However, on this scale, the difference between k_{31} and enhancement was almost significant ($P = .91$).

As a result, k_{31} is shown to be a powerful test criterion for tumor classification. Conditional for the power of the test is that a sufficient accuracy is obtained for this parameter. In our method, as discussed above, such an accuracy could be obtained without observation of the bolus arrival time and with a dynamic scan with a temporal resolution of 30 seconds.

Pharmacokinetic analysis of the data should allow a direct comparison to the results of other groups obtained with similar methods. One of these groups is Hulka et al (21), but from their paper, one can derive that in their patients, the mean value of EF for benign lesions is $3 \cdot 10^{-3}$ sec^{-1} and for malignant lesions $8 \cdot 10^{-3}$ sec^{-1}. This is much lower than the values shown in Table 1 for k_{31} (14 and $35 \cdot 10^{-3}$, respectively). This difference is surprising and may be related to a difference in definition of the enhancing regions. Hulka et al used a threshold for EF of $6 \cdot 10^{-3}$ sec^{-1}. When their threshold is used in Figure 5c, no false negatives and five false positives result, so that this threshold could be defended as suitable for our data (we suggest a threshold of $14 \cdot 10^{-3}$ sec^{-1}).

Hulka et al used a scan method with a very high temporal resolution (6 seconds). Even with their modern echo planar scan technique, this was cause for a rather coarse spatial resolution (pixel size of $7 \times 1.5 \times 3$ mm^{-3}). For tumor classification, they noted for their test a sensitivity of 86% and a specificity of 93%. When testing with k_{31} we found a similar sensitivity of 92% and a somewhat lower specificity of 70%. The difference between the test results may be caused by poor statistics because of the small series used (Hulka et al: 20 patients; our series: 32 patients).

Considering the obtained test results, the relatively low temporal resolution of our scan method seems to be compatible with a high specificity for tumor classification. This means that there is opportunity for a scan with a high spatial resolution. In our system, we reached a spatial resolution of $6 \times 1.3 \times 1.7$ mm^3. Increased system specifications would be desirable in the first place to further improve this spatial resolution. Based on gradient-echo techniques, such improvement could be reached with stronger gradients allowing a short (in-phase) TE of 4.5 msec and a short TR. Echo-planar techniques could bring a moderate further improvement in resolution, although determination of T1 by our dual flip angle method would not be possible.

Interpretation of Obtained Parameters

The pharmacokinetic parameter values found for normal tissue and lesions, as shown in Table 2, can be interpreted, to some extent, as properties of the tissue. This is because these parameters have a biophysics definition and are independent of the MR technique used. The volume fractions f_1 and f_3 of the vascular and leakage space compartment in the voxel as defined in the model and given in Table 2 can be compared with other data. In normal peripheral tissue, the capillary space is 1% (30,31), and in adult females, the extracellular water content is 20% (32). These values are not unlike our values of f_1 and f_3 of normal glandular tissue and fat.

The values of f_1 in benign as well as malignant lesions are higher than those of normal tissue, as shown in Table 2. This may be related to tumor-associated angiogenesis (9,21). Various literature suggests a contribution to the signal enhancement from the vascular residing Gd-DTPA. For

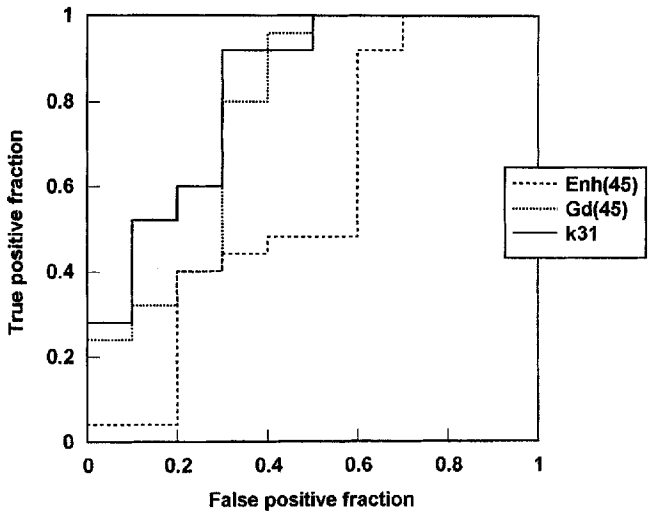

Figure 4. Receiver operating curves for classification of tumors to benign or malignant. Comparison of *Enh(45)*, *Gd(45)*, and k_{31} to histology.

instance, Boetes et al (18) ascribe the onset of their enhancement-time curves as an arterial contribution to the signal. Gilles et al (9) and Hulka et al (21) find a correlation between increased capillary density and tumor enhancement. Moreover, there is direct evidence that in tumorous regions, the size of the vascular space is large. Furman-Haran et al (33) show the presence of localized areas of dense and permeable capillaries in the tumor in their study of MCF-7 human breast tumors implanted in nude mice. In addition, they show the enhancement of such areas in dynamic MRI after Gd-DTPA injection. Shweiki et al (34) conclude that leakage and angiogenesis may occur simultaneously in malignant human tumor tissue.

Table 2 shows that the values of f_3 found in lesions are large as well. The combined occurrence of the elevated values of f_1 and f_3 can explain the high detection sensitivity of contrast-enhanced MRI both for benign and malignant breast lesions.

In conclusion, our data support the notion that malignant breast tumors are characterized by neovascularization and vessel leakage. However, we have no statistical evidence regarding whether such properties will depend on the histologic type of the tumors that were found in our series, nor can we predict the pharmacokinetic behavior of still other types of breast tumors. Neovascularization in malignant tumors could be specifically dependent on f_1 and f_3. Our measurement accuracy was not sufficient to resolve such a dependence. Improved accuracy for f_1 and f_3, could be reached straightforwardly by determination of the bolus arrival time per patient, eg, with a separate fast two-dimensional scan through the

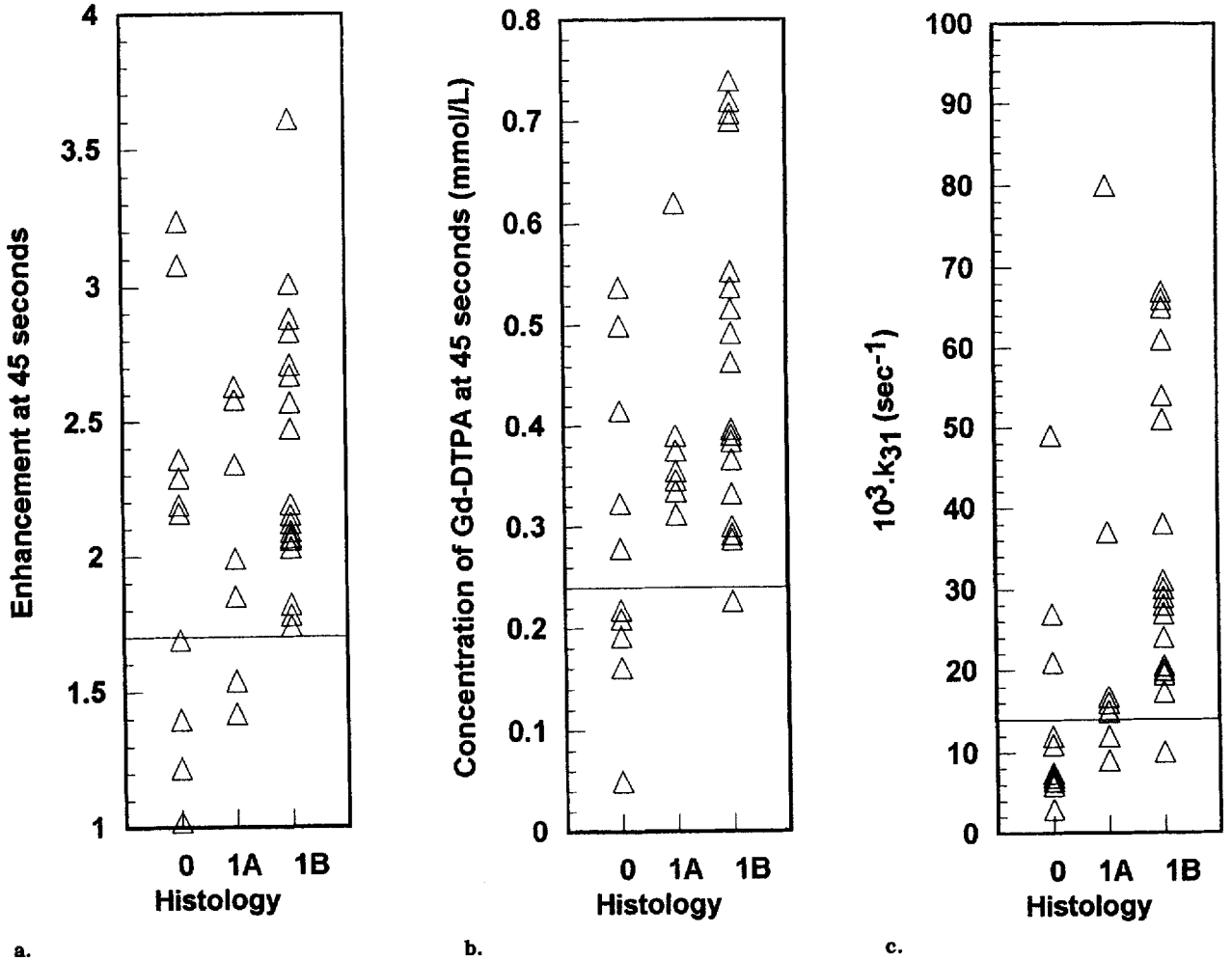

Figure 5. Scatter diagrams for classification of lesions in benign and malignant for some test criteria and suggested thresholds between these classes. The class of malignant lesions is subdivided into in situ lesions (1A) and invasive lesions (1B). **(a)** Enhancement at 45 seconds; threshold for *Enh(45)* = 1.7; **(b)** Gd-DTPA concentration at 45 seconds; threshold for *Gd(45)* = .24 mmol/l. **(c)** Permeability; threshold for $k_{31} = 14 \cdot 10^{-3}$ sec^{-1}.

Table 3
Overview of Enhancing Regions not Corresponding to Lesions Found in X-Ray Mammography (New Lesions)

	Case 10	Case 11	Case 27
Client of mass screening program	no	yes	yes
Hisologic lesion class of mammographically suspected lesion (see Table 1)	0	0	1
Number of new lesions found	4	1	1
Number of new lesions with $k_{31} > 14 \cdot 10^{-3}$ sec^{-1}	3	1	1
Number of lesions in contralateral breast	1	0	1

aortic arch. This could potentially result in an additional increase of the specificity of the test.

In our tumor classification tests, one of the false positives was the same case of fibroadenoma (case 10), which is characterized by a high k_{31}. Apparently, even after our data reduction, fibroadenomas can mimic malignant tumors and can be expected to create false positives in future tests. The false negatives usually included comedo-type ductal carcinoma in situ, of which Gilles et al (9) note that angiogenesis sometimes is weak. Figure 5 suggests that permeability in these tumors may be weak as well. Future tests may have false-negative findings for such lesions. These remarks indicate that MRI based noninvasive testing of breast lesions does not obviate the need for histology.

• CONCLUSIONS

This study shows that our method of scanning, with its moderate spatial resolution and moderate temporal resolution, allowed a sensitive detection of tumors in a region covering both breasts as well as a sensitive and specific classification to malignancy of the tumors detected. The accuracy of classification was shown to be improved by removal of the influence of the native T1 from the data as well as by subsequent pharmacokinetic modeling. The pharmacokinetic permeability k_{31} could be found with an acceptable measurement accuracy (20%).

Based on enhancement, the lesion detection sensitivity was 96%. Classification of tumors with k_{31} was possible with a sensitivity of 92% and a specificity of 70%. The potential value of the proposed method for detection of new malignant tumors not suspicious in x-ray mammography was illustrated by the findings in three patients of six new enhancing regions. Five of these had a value of k_{31} indicating malignant behavior.

The small number of patients tested in this study limits its prognostic value. Additional tests are needed to prove the clinical value of our approach. Improvement of measurement accuracy may be needed to find equal or better specificity in future series. Such improvements can be realized. However, the test accuracy obtained in our study already indicates that the clinical value of our method for patients or clients of population screening with unclear diagnosis or with high risk factors may exist.

• APPENDIX A

Derivation of the Weighted Sum Image

In the dynamic contrast injection studies, contrast enhancement is observable in a number of scans. To emphasize the enhancement, it can be desirable to have access to a single weighted sum image derived from the dynamic scans. Weighted summation can be based on the comparison of the actually observed enhancement factors to their expected values. The method to do this is derived from eigen image filtering theory (26). Per pixel, the enhancement factors can be considered as an N dimensional vector $\underline{\mathbf{p}}$, in which N is the number of dynamic scans. For the dynamic scan described in the main text of this report, Table A1 shows the enhancement factors expected for a malignant lesion (desired tissue property; vector $\underline{\mathbf{d}}$) and those expected for normal glandular tissue (undesired tissue property; vector $\underline{\mathbf{u}}$). These were obtained by averaging the enhancement observed in five patients with malignant lesions (average values of T1: 1,060 msec; k_{31}: $35 \cdot 10^{-3}$ sec^{-1}; f_1: 10%; and f_3: 30%) and in five regions of normal glandular tissue (parameters from Table 2) and smoothing these data. $\underline{\mathbf{d}}$ and $\underline{\mathbf{u}}$ create the weighting factors (vector $\underline{\mathbf{e}}$) for the weighted summation of the enhanced images that maximizes the contrast-to-noise ratio between the desired and the undesired tissue property vectors.

Table A1
Enhancement Factors and Weighting Factors Used for Derivation of the Weighted Sum Images

	Expected Enhancement		
Time (seconds)	Lesion ($\underline{\mathbf{d}}$)	Gland ($\underline{\mathbf{u}}$)	Weighting Factor $\underline{\mathbf{e}}$
0	1	1	−1.16
15	2.02	1.06	−.27
45	2.80	1.15	.32
95	3.06	1.24	.39
175	3.05	1.31	.23
245	3.00	1.32	.14
315	2.95	1.33	.08

$$\underline{\mathbf{e}} = \frac{\underline{\mathbf{d}} \cdot \underline{\mathbf{d}}}{\underline{\mathbf{u}} \cdot \underline{\mathbf{u}}} \cdot \underline{\mathbf{d}} \qquad \text{(A1)}$$

The elements of the vector $\underline{\mathbf{e}}$ are listed in Table A1. For each scan, the pixel values $\underline{\mathbf{c}}$ of the composite image are calculated with $\underline{\mathbf{e}}$ as:

$$\underline{\mathbf{c}} = \underline{\mathbf{e}} \cdot \underline{\mathbf{p}} \qquad \text{(A2)}$$

• APPENDIX B

Conversion of Enhancement to Concentration of Gd-DTPA

For the T1-FFE imaging method, the spoiled gradient-echo sequence available on our system, the signal strength s is shown theoretically and experimentally verified by Van der Meulen et al (35) to be given by:

$$s = M_0 \sin \alpha \frac{(1 - \exp(-TR/T1))\exp(-TE/T2^*)}{1 - \cos \alpha \exp(-TR/T1)} \qquad \text{(B1)}$$

When two T1-FFE scans are performed, each with a different flip angle, as proposed in refs. 16 and 36, the derivation of T1 is possible from this equation. The value obtained is that of $T1_N$, the native value of T1 before administration of Gd-DTPA. Rewriting Equation [B1] shows this for signals s_α and s_β, obtained with flip angles α and β:

$$T1_N = TR/\ln\left(\frac{s_\alpha \sin\beta \cos\alpha - s_\beta \sin\alpha \cos\beta}{s_\alpha \sin\beta - s_\beta \sin\alpha}\right) \qquad \text{(B2)}$$

The change in relaxation time during the dynamic scan

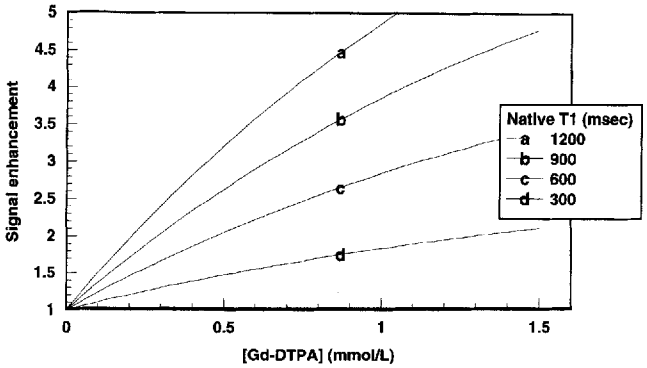

Figure B1. Signal enhancement as a function of the tissue concentration of Gd-DTPA, calculated from Equations [B1] and [B2] for tissues with different native T1 in a three-dimensional FFE sequence with TR = 16, TE = 9, flip angle = 40; $r_1 = 4.5$ l mmol^{-1} sec ^{1}; $r_2^* = 5.5$ l mmol^{-1} sec^{-1}. This figure shows that enhancement is an approximately linear function of the concentration but, in addition, is almost linearly dependent on native T1.

is caused by the tissue concentration of Gd-DTPA. Equation [B3] is the experimental result taken from Weinmann et al (37) and holds over the range of Gd-DTPA concentrations occurring in clinical practice; 0 to 2 mmol/l:

$$\frac{1}{T1} = \frac{1}{T1_N} + r_1 C_t$$
$$\frac{1}{T2} = \frac{1}{T2_N} + r_2^* C_t \qquad \text{(B3)}$$

with r_1 and r_2^* the relaxivities (l mmol^{-1} sec^{-1}) and C_t the average value of concentration of the contrast medium taken over all tissue in the voxel (mmol l ^{1}). When the dynamic series starts with a scan before arrival of the contrast medium, its concentration can, with the help of Equations [B1] and [B3], be found from the enhancement factor, if the native T1 is known.

The overall effect of the influx of contrast medium in practical concentrations is an increase in signal intensity because of T1 shortening. This relation is illustrated in Figure B1. As expected, the enhancement factor is roughly proportional to concentration. At much higher concentrations, T2* shortening will become dominant and the enhancement will saturate. The figure shows, in addition, that for a given concentration, the enhancement factor is larger when the native T1 is longer. This last effect is due to the low signal strength in the precontrast images in regions with a long T1.

• APPENDIX C

Pharmacokinetic Model

The behavior of Gd-DTPA after its injection as a bolus into the human body is described as an exchange of Gd-DTPA between the compartments shown in Figure C1. After its introduction, the contrast medium will distribute rapidly in the plasma within the early distribution volume V_1 (38).This volume roughly corresponds to that of the plasma in the vascular volume and is loosely referred to as "vascular space" in the remainder of this paper. The concentration in this compartment then drops off gradually because of diffusion into the leakage space of the body with volume V_2. This model is similar to what is used in pharmacy to describe the distribution of drugs (39). For that reason, the model may be called a "pharmacokinetic model." For the purpose of analysis, this leakage space is thought of as divided into two spatially separate compartments, one of which, the voxel leakage space (volume V_3), is located in the voxel under consideration. The compartments exchange Gd-DTPA with transfer coefficients k_{ij}. Clearing from the vascular compartment via the kidney takes place as well and has a transfer coefficient k_{10}.

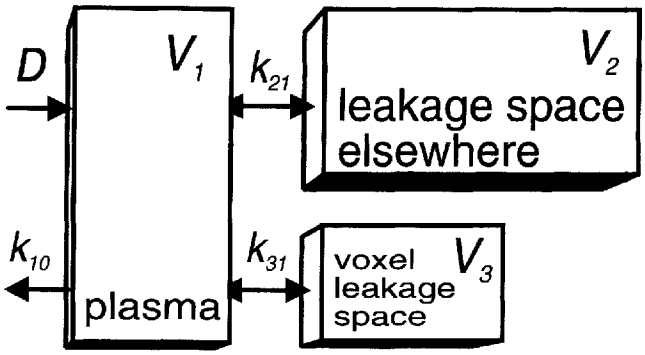

Figure C1. Three-compartment model, used for pharmacokinetic modeling of the concentration of Gd-DTPA as a function of time.

The continuity equations that describe the exchange of matter between these compartments for a situation of passive concentration driven transport can be expressed as equations for the concentrations C_i:

$$\dot{C}_1 = -k_{10}C_1 + k_{21}\frac{V_2}{V_1}(C_1 - C_2) + k_{31}\frac{V_3}{V_1}(C_3 - C_1)$$
$$\dot{C}_2 = k_{21}(C_1 - C_2) \qquad \text{(C1)}$$
$$\dot{C}_3 = k_{31}(C_1 - C_3)$$

The transfer coefficients k_{ij} have the dimension t^{-1} and are formally described as the mean permeability surface area product per unit volume of compartment i. Tofts et al (20) introduced for these coefficients the term "permeability," which convention we will follow.

The third term in the first of these equations can be neglected because of the very small value of the ratio V_3/V_1. When a dose D is injected at $t = 0$, C_1 is assumed to step up immediately to its initial value D/V_1. Equation [C1] can then be solved. In Figure C2, curves a and b, the obtained solutions for C_1 and C_3 are shown graphically for a typical set of parameters. As can be seen, C_1 has an initial value 1 and an approximately exponential decrease. C_3 starts at zero and shows washin first. After its peak concentration has been reached, the washout is at a rate that closely follows that of C_1.

Within a voxel, vascular space as well as leakage space will always be present and each will occupy a fraction of the total voxel volume. These fractions will be called f_1 and f_3. The average concentration of Gd-DTPA in the voxel, C_t, is the weighted sum of the concentrations in each volume fraction:

$$C_t = f_1 C_1 + f_3 C_3 \qquad \text{(C2)}$$

The MR signal is assumed to be a function of C_t. This is true when there is fast exchange of spins between the compartments. Fast between cellular and extracellular space is expected (40). It is reasonable as well to assume its existence between the capillaries and the vascular space, considering the open structure of the capillaries

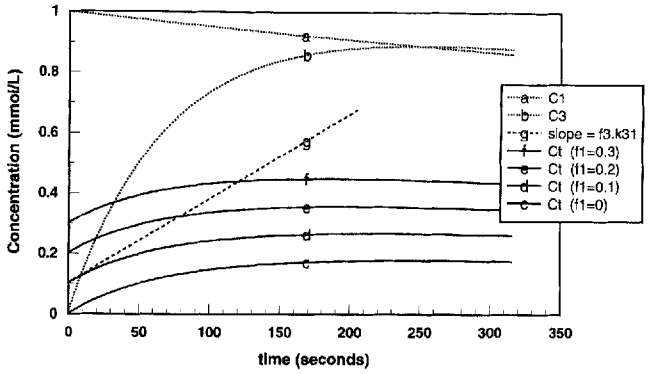

Figure C2. Theoretical concentration-time curves of Gd-DTPA after bolus injection. Parameters are: D = 7.5 mmol, V_1 = 7.5 l, V_2 = 16.6 l, k_{21} = .51 × 10^{-3} sec^{-1}, k_{31} = 20 · 10^{-3} sec^{-1}, f_3 = .1. (**a**) Gd-DTPA concentration in plasma space. (**b**) Concentration in leakage space. (*c*) through (*f*): Concentration-time curves as would be observed by MRI for a plasma space f_1 of 0, 10, 20, and 30%. (*g*) Straight line showing the initial slope of curve *d* to be equal to $f_3 \cdot k_{31}$.

in the visceral space (41). Equation [C2] therefore connects the physics of MRI to that of pharmacokinetics.

The modeled behavior of C_t is shown in Figure C2 (solid curves) for some values of f_1. The step of C_t at t = 0 is proportional to f_1; its increase then continues, starting at a slope $f_3 \cdot k_{31}$, which reflects the washin into the voxel leakage space, until the peak concentration is reached. As shown in the figure, the peak in C_t is reached earlier than that in C_1, especially for large f_1.

The output parameters of the model govern the shape of the concentration-time curves. These parameters are f_1, f_3, and k_{31}. Together with $T1_N$ and the actual MRI scan parameters, they describe the shape of the enhancement-time curve as well.

In our use of the model, a number of parameter values were assumed from the literature. These values and their assumed precision for the in vitro situation in the patient are listed in Table C1.

For the relaxivities r_1 and r_2^* of Gd-DTPA, we have used literature values observed by Tofts et al (42) in gradient-echo experiments in gels at 1.5 T. The parameters V_1, V_2, k_{21}, and k_{10}, governing the decay of the plasma concentration of Gd-DTPA after bolus injection are based on experimental observations in plasma samples obtained from volunteers. These experiments of Weinmann (39) show a biexponential decay of the plasma concentration. The resulting values of the transfer coefficients follow from a mathematical reformulation.

Table C1
Assumed Parameter Values of the Pharmacokinetic Model

Relaxivities of GD-DTPA in tissue	r_1 = 4.5	$l\ mol^{-1}\ sec^{-1}$	(42)
	r_2^* = 5.5	$l\ mol^{-1}\ sec^{-1}$	(42)
Vascular space	V_1 = .12	l/kg	(43)
Leakage volume elsewhere in the body	V_2 = .27	l/kg	(43)
Transfer coefficients	k_{10} = .23·10^{-3}	sec^{-1}	(43)
	k_{21} = .51·10^{-3}	sec^{-1}	(43)
Transport time of Gd-DTPA in the body	tt = 15	sec	(28)

• APPENDIX D

Errors in the Parameters Obtained from the Pharmacokinetic Model

The errors in the derived parameters are the result of application of the fitting procedure to imperfect input data. Therefore, an estimate of the errors in the input parameters has to be given first. Such estimates are discussed below and summarized in column 2 of Table D1. An estimate of the resulting output errors can be obtained by observing the propagation of input errors in the fitting procedure for representative sets of input data (20). We have applied this manner of error estimation in five actual input data sets in which the size of the enhancing regions ranged from 10 to 40 pixels and k_{31} from 11 to 44 · 10^{-3} sec^{-1}. The input parameters were varied individually over their error range and the ranges of the resulting output errors are shown in Table D1, columns 3 through 5. The estimated total error per parameter is obtained by quadratic addition of the error terms and is given at the bottom row of these columns.

The following input errors were considered:

- Error in the experimental values of T1. Experimental assessment of the accuracy of determination of T1 with our method (dual flip angle T1-FFE) was obtained with help of a phantom with calibrated values of T1 (43). In the range of T1 values of 200 to 1,000 msec, the phantom data were shown to be accurate within 5%. The clinical situation is less favorable. T1 decay may not be monoexponential and, in the large field of view used, the transmit coil may not be sufficiently homogeneous. A visual impression of the accuracy of T1 over the transverse breast images is given in Figure 1c, a parameter image of T1. T1 of the fat is constant over most of the field of view and much better than the signal in the unprocessed images 1a and b. Nevertheless, the T1 values obtained will be approximate only. Their accuracy is expected to be only approximately 15%.
- Movement of the patient between the dynamic scans was corrected by in-plane shifting of the images. After reregistration, the remaining in-plane error of movement was estimated to be less than .3 pixels. The movement perpendicular to the imaging plane is estimated to be less than 2 mm. The error in the data from patient movement was considered negligible and is not shown.
- Movement of the patient (presumably mainly respiratory motion) during each dynamic scan was cause of a slight ghost, visible for instance in the background of Figure 1a. The intensity of the ghost was a few percent of the scale maximum. For error analysis, it was assumed to behave as random noise.
- Image noise in the MRI data from the dynamic scans. The range of the thermal noise per pixel was observed to be smaller than 1% (2/.655 times the SD in a ghost-free background image region, compared with the scale maximum). Ghost and thermal noise together were estimated to have a range of 2% of the scale maximum.
- Intravoxel inhomogeneity was not observed directly. For small enhancing regions, partial volume effects during the dynamic scans can become an important reason for intravoxel inhomogeneity, which then may degrade the meaning of the parameter estimates. The restriction that was imposed for the minimum size of the enhancing region (eight pixels) reduces this influence of partial volume effects. The error caused by intravoxel inhomogeneity was estimated by increasing the voxel size in the test data sets with a factor of 2 and repeating the analysis.

Table D1
Error Sources and Error Propagation to Output Parameters

Error Sources	Error Range (2 SD)	Output Parameter Error Per Source (%)		
		f_1	f_3	k_{31}
$T1_N$	+/−15%	9	12	2
Image noise	+/−2%	6	14	14
Intra-voxel inhomogeneity	×2	6	7	8
V_1	+/−20%	20	20	0
r_1	+/−20%	20	20	0
r_2*	+/−50%	5	5	0
V_2	+/−20%	9	9	0
k_{21}	+/−20%	9	9	0
k_{10}	+/−20%	9	9	0
tt	+/−10 seconds	32	22	12
Total error in output parameters (2 SD):		45%	41%	20%

- The value for pharmacokinetic input parameters V_1, r_1, r_2*, V_2, k_{21}, and k_{10} were assumed to be accurate within 20% with the exception of r_2*, which is likely to be less accurate (44), so we assumed 50% accuracy for that parameter.
- The range of transport times tt of the contrast medium from the place of injection to the breast was estimated from the data of Kruger (25) to be 15 ± 10 seconds. These data show, in addition, that the front edge of the bolus is not a step function but has a rise time of approximately 6 seconds. The influence of this finite rise time on the analysis was neglected in comparison with the temporal resolution of the dynamic scan (30 seconds).

Acknowledgments: The authors thank Peter Oosterhof, who thoroughly reviewed the mathematics, Tom Peters and Aaldert Elevelt, for their helpful and stimulating discussions, and Francis Welhuis and Sander Wansing, for their assistance in working out the data.

References

1. Kaiser WA, Zeitler E. MR imaging of the breast: fast imaging sequences with and without Gd-DTPA. Radiology 1989; 170: 681–686.
2. Stack JP, Redmond OM, Codd M, Dervan PA, Ennis JT. Breast disease: tissue characterization with Gd-DTPA enhancement profiles. Radiology 1990; 174:491–494.
3. Lewis Jones HG, Whitehouse GH, Leinster SJ. The role of MR imaging in the assessment of local recurrent breast carcinoma. Clin Radiol 1993; 43:117–204.
4. Klengel S, Hietschold V, Schreiber M, Kohler K. Quantitative kontrastmitteldynamische mamma-MRT am 0.5 Tesla gerät. Rontgenpraxis 1994; 47:223–228.
5. Flickinger FW, Allison JD, Sherry RM, Wright JC. Differentiation of benign from malignant breast masses by time intensity. Magn Reson Imaging 1993; 11:617–620.
6. Turkat TJ, Klein BD, Polan RL, Richman RH. Dynamic MR mammography. A technique for potentially reducing the biopsy rate for benign breast disease. J Magn Reson Imaging 1994; 4:563–568.
7. Stomper PC, Herman S, Klippenstein DL, et al. Suspect breast lesions: findings at dynamic gadolinium enhanced MR imaging correlated with mammographic and pathologic features. Radiology 1995; 197:387–395.
8. Hickman PF, Moore NR, Shepstone BJ. The indeterminate breast mass: assessment using contrast enhanced magnetic resonance imaging. Br J Radiol 1994; 67(793):14–20.
9. Gilles R, Zafrani B, Guinebretiere JM, et al. Ductal carcinoma in situ: MR imaging — histopathologic correlation. Radiology 1995; 196:415–419.
10. Frouge C, Guinebretiere JM, Contesso G, Di Paola R, Blery M. Correlation between contrast enhancement in dynamic MRI of the breast and tumour angiogenesis. Invest Radiol 1994, 29:1043–1049.
11. Heywang SH, Wolf A, Pruss E, Hilbertz T, Eiermann W, Permanetter W. MR imaging of the breast with Gd-DTPA: use and limitations. Radiology 1989; 171:95–103.
12. Harms SE, Flamig DP. MR imaging of the breast. J Magn Reson Imaging 1993; 3:277–283.
13. Rigauts H, Casselman J, Steyart L, Devlies F, Pattijn G. Contribution of MRI and colour doppler Sonography in breast cancer. J Belge Radiol 1993; 76:226–231.
14. Greenstein Orel S, Schnall MD, Levels V, Trepan RH. Suspicious breast lesions: MR imaging with radiologic-pathologic correlation. Radiology 1994; 190:485–493.
15. Perman WH, Heiberg EM, Grunz J, Herrmann VM, Janney CG. A fast 3D-imaging technique for performing dynamic Gd-enhanced MRI of breast lesions. Magn Reson Imaging 1994; 12:545–551.
16. Den Boer JA, Dornseiffen G, Elevelt A, et al. Quantitative 3D temporal tracking of redistribution of Gd-DTPA in the mamma (abstract). J Magn Reson Imaging 1993; 4:90.
17. Smink J, den Boer JA, Dornseiffen G, et al. Breast lesion differentiation based on the pharmacokinetic behavior of Gd-DTPA. J Magn Reson Imaging 1994; 4:90.
18. Boetes C, Barentsz JO, Mus RD, et al. MR characterization of suspicious breast lesions with a gadolinium-enhanced TurboFLASH subtraction technique. Radiology 1994; 193: 777–781.
19. Gribbestad IS, Nilsen G, Fjosne HE, Kvinnsland S, Haugen OA, Rinck PA. Comparative signal intensity measurements in dynamic gadolinium-enhanced MR mammography. J Magn Reson Imaging 1994; 4:477–480.
20. Tofts P, Berkowitz B, Schnall MD. Quantitative analysis of dynamic Gd-DTPA enhancement in breast tumors using a permeability model. Magn Reson Med 1995; 33:564–568.
21. Hulka PS, Smith BL, Sgroi DC, et al. Benign and malignant breast lesions: differentiation with echo-planar MR imaging. Radiology 1995; 197:33–38.
22. Tofts PS, Kermode AG. Measurement of the blood-brain barrier permeability and leakage space using dynamic MR imaging. 1. Fundamental concepts. Magn Reson Med 1991; 17: 357–367.
23. Hess T, Knopp MV, Hoffmann U, et al. A pharmacokinetic analysis of Gd-DTPA enhancement in MRT in breast carcinoma. Rofo Fortschr Geb Rontgenstr Neuen Bildgeb Verfahr 1994; 160:518–523.
24. Hoffmann U, Brix G, Knopp MV, Hess T, Lorenz WJ. Pharmacokinetic mapping of the breast: a new method for dynamic MR mammography. Magn Reson Med 1995; 33:506–514.
25. Kruger RA, Riederer S, eds. Basic concepts of digital subtraction angiography. Boston: G.K. Hall, 1984;210–217.
26. Windham JP, Abd-Allah MA, Reimann DA, Froelich JW, Haggar AM. Eigenimage filtering in MR imaging. J Comput Assist Tomogr 1988; 12:1–9.
27. Press WH, Flannery BP, Teukolski SA, Vetterling WT, eds. Modelling of data. In: Numerical recipes in C, the art of scientific computing. Cambridge University Press, Cambridge, UK, 1988; 517–565.
28. Hanley JA, McNeil BJ. A method of comparing the areas under receiver operating characteristic curves derived from the same cases. Radiology 1983; 148:839–843.
29. Hanley JA, McNeil BJ. The meaning and use of the area under a receiver operating characteristic (ROC) curve. Radiology 1982; 143:29–36.
30. Ganong WF. The general and cellular basis of medical physiology. In: Ganong WF, ed. Review of medical physiology. Norwalk, CT: Appleton & Lange, 1989; 1–2.
31. Schmidt RF, Thews G. Human physiology. New York: Springer Verlag, 1983.
32. International Commission on Radiation Protection. Report of the task group on reference man. ICRP publication 23. Oxford: Pergamon Press, 1975; 32.
33. Furman-Haran E, Margalit R, Grobgeld D, Degani H. Dynamic contrast-enhanced magnetic resonance imaging reveals stress-induced angiogenesis in MCF7 human breast tumors. Proc Natl Acad Sci USA 1996; 93:6247–6251.
34. Shweiki D, Itin A, Soffer D, Keshet E. Vascular endothelial growth factor induced by hypoxia may mediate hypoxia-initiated angiogenesis. Nature 1992; 359:843–845.
35. Van der Meulen P, Groen JP, Tinus AMC, Bruntink G. Fast field echo imaging: an overview and contrast calculations. Magn Reson Imaging 1988; 6:355–368.
36. Wang HZ, Riederer SJ, Lee JN. Optimizing the precision in T1 relaxation estimation using limited flip angles. Magn Reson Med 1987; 5:399–416.

37. Weinmann HJ, Brasch RC, Pres WR, Wesby GE. Characteristics of gadolinium-DTPA complex: a potential NMR contrast agent. AJR Am J Roentgenol 1984; 42:619–624.
38. Weinmann HJ, Laniado M, Mützel W. Pharmacokinetics of Gd-DTPA/dimeglumine after intravenous injection into healthy volunteers. Physiol Chem Phys Med NMR 1984; 16: 167–172.
39. Roland M, Thosar TN. Clinical pharmacokinetics, concepts and applications. Philadelphia: Lea & Febiger, 1980.
40. Koenig SH, Spiller M, Brown RD, et al. Relaxation of water protons in the intra and extra cellular regions of blood containing Gd(DTPA). Magn Reson Med 1986; 3:791–795.
41. Bassingthwaighte JB. Microcirculatory considerations in NMR flow imaging. Magn Reson Med 1990; 14:172–178.
42. Tofts PS, Shuter B, Pope JM. Ni-DTPA doped agarose gel — a phantom material for Gd-DTPA enhancement. Magn Reson Imaging 1993; 11:125–133.
43. Lerski RA, McRobbie DW, de Certaines JD. Protocols and test objects for the assessment of MRI equipment. Magn Reson Imaging 1988; 6:195–199.
44. Gore JC, Majumdar S. Measurement of tissue blood flow using intravascular relaxation agents and magnetic resonance imaging. J Magn Reson 1988; 78:41–55.

Announcements of Meeting

New Developments in Contrast Agent Research, 6th Special Topic Seminar on MR Contrast Agents, Schloss Fuschl, Salzburg, Austria; June 3–5, 1998. Contact Prof. Dr. Robert N. Muller; EMRF Foundation, Belgian Office; University of Mons-Hainaut; NMR Laboratory; B-7000 Mons; Belgium; Telephone: +32 65 37 3520; Telefax: +32 65 37 3521. The number of participants is limited.